Ultramicroscopy 41 (1992) 387–397
North-Holland

ultramicroscopy

Crystal structure determination of $K_2O \cdot 7Nb_2O_5$ by combining high-resolution electron microscopy and electron diffraction

J.J. Hu, F.H. Li and H.F. Fan

Institute of Physics, Chinese Academy of Sciences, Beijing 100080, People's Republic of China

Received 1 October 1991; in final form 19 December 1991

With an image deconvolution procedure based on the principle of maximum entropy, positions of metallic atoms in crystal of $K_2O \cdot 7Nb_2O_5$ have been determined from a single high-resolution electron microscope image and from the combination of the image and the electron diffraction pattern. The function of image deconvolution is to transform an image taken under an arbitrary defocus condition into the structure image. The structure images restored from two original images taken under much different defocus conditions show almost the same contrast. In the restored structure images, niobium and potassium atoms appear as black dots with larger and smaller contrast, respectively. The positions of oxygen atoms have been determined by the phase-extension technique developed in X-ray crystallography. Moduli of structure factors up to $H = 1$ Å^{-1} were obtained from the electron diffraction pattern, while phases within $H \leq (1.9$ Å$)^{-1}$ were derived from Fourier transform of the electron microscope image after deconvolution. The Sayre equation was used to extend the phase from (1.9 Å$)^{-1}$ to 1 Å^{-1} and to retrieve the phases of those reflections within (1.9 Å$)^{-1}$, which were rejected in image deconvolution owing to unreliable values of the contrast transfer function. Fourier synthesis was used to improve the quality of the image after phase extension. The final structure image reveals clearly all atoms in the unit cell.

1. Introduction

The crystal of $K_2O \cdot 7Nb_2O_5$ grown by the Czochralski method [1] is exclusively found in paragenesis with other potassium–niobium oxides. The period along one of the crystallographic axes is very short. Hence, high-resolution electron microscopy (HREM) has the advantage of determining the crystal structure.

The crystal structure determination in HREM is usually performed by using trial-and-error methods. With this kind of method the structure under examination should be partially known in advance so that the optimum defocus image, i.e. the structure image which reflects the projected crystal structure, can be recognized among the series of images taken under different defocus conditions. One or more structure models can be proposed based on the contrast of the optimum defocus image and the correct structure model is chosen by comparing the series of experimental images with simulated images. However, the method might not be successful when the sample is easily damaged under the electron beam irradiation or the structure under investigation is entirely unknown beforehand.

The image processing provides another approach to crystal structure determination in HREM. It contains two steps: image deconvolution and image resolution enhancement [2]. The goal of image deconvolution is to transform the images taken at any defocus condition into the structure image so that the projected crystal structure can be obtained. Different methods have been developed for image deconvolution [3–15]. Structure details contained in the structure image so obtained will be limited by the resolution of the electron microscope. It was reported that the

0304-3991/92/$05.00 © 1992 – Elsevier Science Publishers B.V. All rights reserved

resolution of structure images can be enhanced by phase extension techniques developed in X-ray crystallography [16–19] so that the resolution of the final structure image can be beyond the limit of the electron microscope. The phase extension technique was successfully applied to enhance the image resolution of chlorinated copper phthalocyanine from 2 to 1 Å by combining the information from the image and from the corresponding EDP so that all atoms including carbon and nitrogen can be seen clearly in the final structure image [19]. The goal of this paper is to determine the positions of metallic atoms in a crystalline $K_2O \cdot 7Nb_2O_5$ sample by image deconvolution and then to determine the position of oxygen atoms by phase extension. This is the first attempt to determine in detail an unknown crystal structure by combining HREM and electron diffraction and by using image processing consisting of image deconvolution and resolution enhancement.

2. Experiment

2.1. Electron microscope observation

The crystals were crushed in an agate mortar. The fine fractures were transferred to a copper grid covered with holey carbon film and examined with an H-9000 electron microscope at the accelerating voltage of 300 kV. The electron diffraction observation was carried out with the microscope equipped with a side-entry goniometer. A series of EDP's were taken with different exposure from the same area of a sample which was selected as thin and flat as possible. A series of high-resolution electron microscope images were taken under different defocus conditions from another sample with the microscope equipped with a top-entry goniometer [20]. The spherical aberration coefficient of the objective lens is 0.9 mm and the resolution of the microscope is 1.9 Å. The sample was always observed with the incident beam parallel to the shortest axis (c axis) which equals to 3.94 Å [1,21]. The electron-optic magnification is 400 000 × or 500 000 ×

2.2. Image digitization and diffraction intensity measurement

Two images which have almost reversed contrast to each other were scanned by a Perkin-Elmer PDS microdensitometer with a raster size of 10 μm × 10 μm which is fine enough to preserve the information to 1.9 Å resolution. The scanned areas in images consist of eight (2 × 4) and ten (2 × 5) unit cells respectively. The digitized images were averaged by considering the image symmetry determined from the EDP and by superimposing different unit cells.

Five EDP's taken with different exposures were measured with the same microdensitometer. Each diffraction spot consists of 3 × 3 or 5 × 5 pixels depending on the spot size. A density–intensity characteristic curve (D–log I) is obtained from the measurement results for the five EDP's. Only those density values which fall in the linear part of the D–log I curve were used for calculating the integral diffraction intensity. The background was deduced from the integral intensity one by one for all diffraction peaks.

3. High-resolution images

Fig. 1 shows two images projected along the c axis together with the corresponding EDP. Their defocus amounts differ greatly from each other. Both EDP's show the 4 mm symmetry. The lattice parameters determined from the EDP's are $a = b = 27.5$ Å. Figs. 2a and 2b show the images enlarged from the thin region of figs. 1a and 1b, respectively. The square frames in the two images denote the projections of an unit cell. There are four flower-shaped white dots consisting of seven petals inside the unit cell shown in fig. 2a. Their positions are coincident to those of the four large white dots in fig. 2b. All the dark dots in fig. 2a correspond to the small white dots in fig. 2b. Both images have the symmetry of P4gm which consists of two-fold axes, four-fold axes, mirror

planes and glide planes as shown in fig. 2c. Because the two images almost have a contrast reversed to each other, it is difficult to judge which one is closer to the projected structure. The image deconvolution has been carried out on both of them separately.

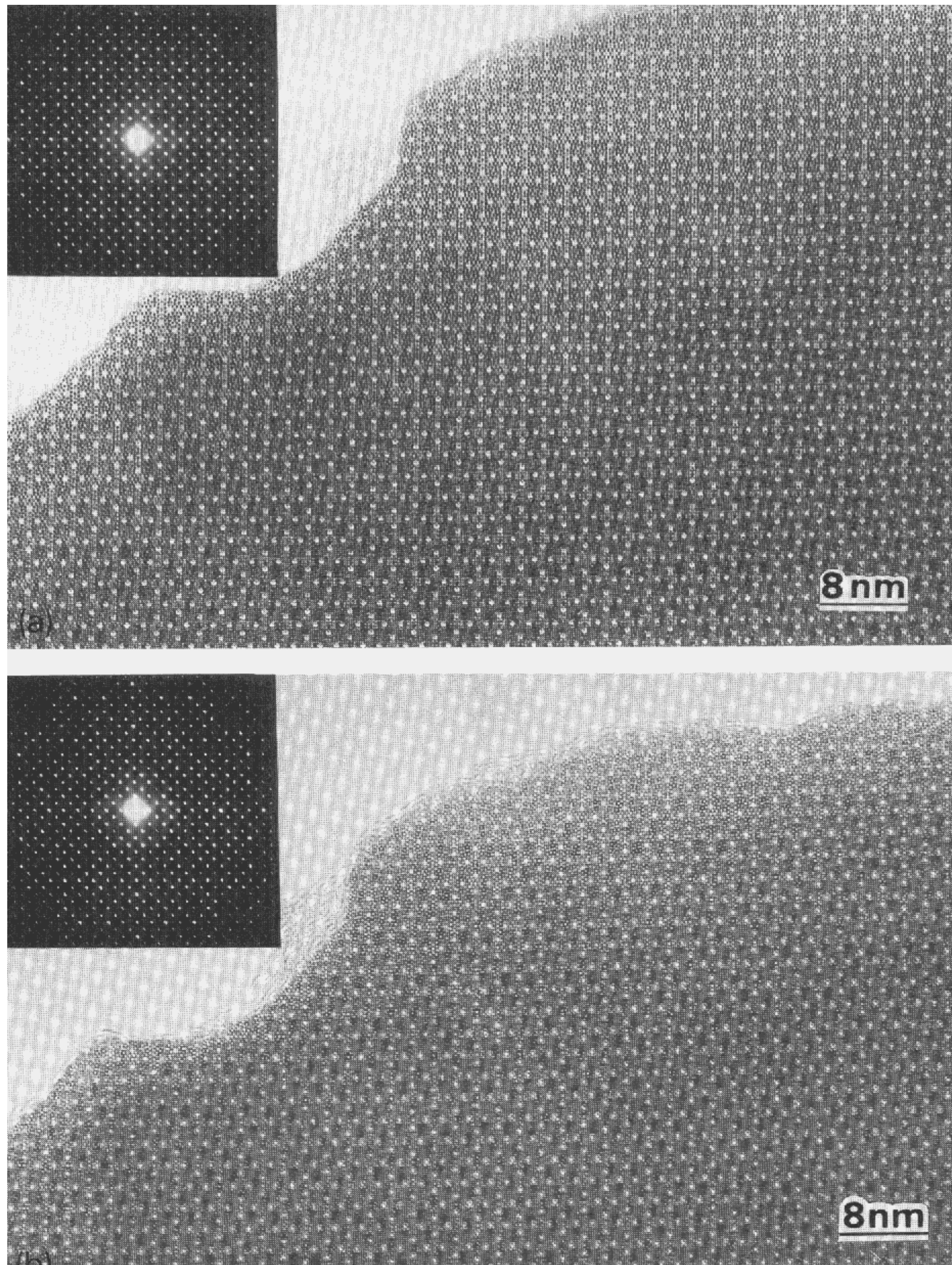

Fig. 1. High-resolution electron microscope images of $K_2O \cdot 7Nb_2O_5$ projected along the c axis together with the corresponding EDP taken by a H-9000 electron microscope at the accelerating voltage of 300 kV. (a) Electron-optic magnification 400000×. (b) Electron-optic magnification 500000×.

4. Determination of metallic atoms by image deconvolution

4.1. Modification of maximum entropy method in image deconvolution

The principle of image deconvolution by the maximum entropy method was introduced and a test of the method was done for simulated images of chlorinated copper phthalocyanine treated as a weak-phase object and as a pseudo-weak-phase object [15]. Under the weak-phase object approximation the image intensity is expressed as

$$I(\boldsymbol{r}) = 1 + 2\sigma\phi(\boldsymbol{r}) * \mathscr{F}^{-1}[W(H)], \qquad (1)$$

where $\phi(\boldsymbol{r})$ denotes the projected potential distribution function and $W(H)$ the contrast transfer function (CTF), $\sigma = \pi/\lambda U$, λ is the wave length, U the accelerating voltage of electrons, $*$ is the operator of convolution and $\mathscr{F}^{-1}$ the operator of inverse Fourier transform (FT). All the parameters in $W(H)$ are more or less known except the defocus amount. The essential of image deconvolution by the maximum entropy method is to assign a series of trial defocus amounts Δf_{trial}, from each of which a trial projected potential distribution map (PPDM) is calculated. The PPDM corresponding to a maximum entropy is selected as the correct one [22]. Although the examined samples generally deviate greatly from a weak-phase object, most of them can be treated as a pseudo-weak-phase object [23]. Hence, the proposed method can still be used only if the projected potential distribution function is replaced by a modified PPDF where the peak

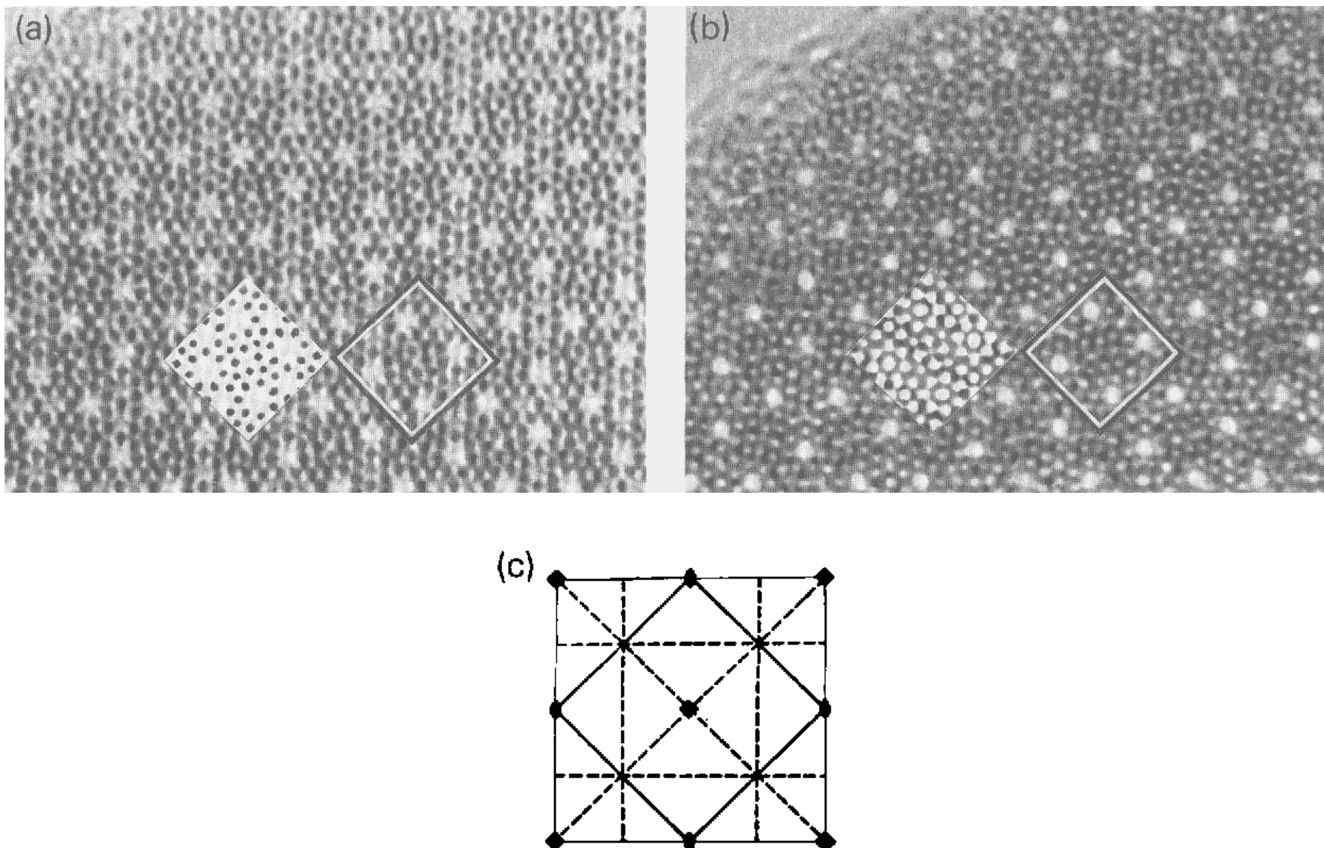

Fig. 2. (a) Image of $K_2O \cdot 7Nb_2O_5$ enlarged from the thin region of fig. 1. (b) Image of $K_2O \cdot 7Nb_2O_5$ taken at the same sample area as (a) but with different defocus condition. The square frames in the two images denote the projections of an unit cell. Both images have the symmetry of P4gm. The simulated images based on the structure model determined by image deconvolution and image resolution enhancement are inserted in the bottom left. (c) The diagram of symmetry elements shows the four-fold axes, mirror planes and glide planes of two-dimensional space group P4gm.

heights of heavy atoms decrease and those of light atoms increase relatively.

One of the problems in image deconvolution for experimental images is the existence of spurious peaks in the trial PPDM's, which lead to a false value of entropy and hence to a wrong Δf_{trial}. This is solved by introducing a constraint to the entropy of projected potential such that the expression of entropy becomes:

$$S = - \sum_{\substack{i=1 \\ P_i > P_c}}^{N} P_i \ln P_i, \tag{2}$$

and

$$P_i = \phi_i / \sum_{i=1}^{N} \phi_i, \tag{3}$$

where $\phi_i = \phi(\boldsymbol{r}_i)$ denotes the value of projected potential on the pixel at $\boldsymbol{r}_i$ and N the total number of pixels inside the unit cell; in the present case $N = 64 \times 64$. P_c is assigned equal to one half of the peak height of the projected potential for an oxygen atom, the lightest atom in $K_2O \cdot 7Nb_2O_5$. The ratio of the potential peak height for a niobium atom to that for an oxygen atom can be obtained from the FT's of the atomic scattering factors of the two atoms. The value of P_c was estimated by taking the maximum value in the trial PPDM as the potential peak height of a niobium atom.

4.2. The moduli of structure factors

Another problem in image deconvolution for experimental images is how to obtain reliable absolute values of structure factors $F(\boldsymbol{H})$. Liu et al. [14] proposed a method of image deconvolution for a single image taken near the Scherzer defocus condition on the basis of Wilson statistics in X-ray crystallography [24]. According to this method the structure factors including the amplitudes and phases can be obtained from the image. This method can also be used to determine the amplitudes of structure factors from an image taken at any defocus condition. From eq. (1), the FT of the image intensity is expressed as

$$T(\boldsymbol{H}) = \delta(H) + 2\sigma F(\boldsymbol{H}) W(H), \tag{4}$$

where $\delta(H)$ denotes the Dirac-delta function and $F(\boldsymbol{H})$ the structure factor. For $H \neq 0$ we have

$$F(\boldsymbol{H}) = T(\boldsymbol{H}) / 2\sigma W(H). \tag{5}$$

The average of $|F(\boldsymbol{H})|^2$ within a narrow ring in the reciprocal plane with a mean radius equal to H can be written as

$$\langle |F(\boldsymbol{H})|^2 \rangle_H \simeq \langle |T(\boldsymbol{H})|^2 \rangle_H / 4\sigma^2 W^2(H). \tag{6}$$

Another expression for the average of $|F(\boldsymbol{H})|^2$ is well known in X-ray crystallography [24]; it is

$$\langle |F(\boldsymbol{H})|^2 \rangle_H \simeq \sum_{j=1}^{N} f_j^2(H), \tag{7}$$

where $f_j(H)$ is the atomic scattering factor of the jth atoms and N the number of atoms in the unit cell. By combining eqs. (5), (6) and (7) the modulus of structure factor can be expressed as [14]:

$$|F(\boldsymbol{H})| = |T(\boldsymbol{H})| \left[\frac{\sum_{j=1}^{N} f_j^2(H)}{\langle |T(\boldsymbol{H})|^2 \rangle_H} \right]^{1/2}. \tag{8}$$

In the present case each $|T(\boldsymbol{H})|^2$ is averaged with ten neighbors (five on each side) to give the value of $\langle |T(\boldsymbol{H})|^2 \rangle_H$. Such obtained $|F(\boldsymbol{H})|$ can be used for image deconvolution performed with a single image. An alternate method of obtaining $F(\boldsymbol{H})$ is to calculate it from the electron diffraction intensity treated on the basis of Wilson statistics [24]. The electron diffraction intensity of each peak $I(\boldsymbol{H})$ was averaged with ten neighbors as above mentioned to obtain $\langle |I(\boldsymbol{H})| \rangle_H$. The modulus of structure factor is determined as

$$|F(\boldsymbol{H})| = \sqrt{I(\boldsymbol{H})} \left[\frac{\sum_{j=1}^{N} f_j^2(H)}{\langle |I(\boldsymbol{H})| \rangle_H} \right]^{1/2}. \tag{9}$$

In such case the image deconvolution is based on the combination of information from an image

and the corresponding EDP. Namely, the trial PPDM's are calculated by using the phases of structure factors obtained from the Fourier transform of the image and the moduli obtained from the EDP. In the following results of image deconvolution performed by using a single image and by combining an image with the EDP for the two experimental images of $K_2O \cdot 7Nb_2O_5$ are described. In all cases the structure information with $|\sin \chi_1 \exp(-\chi_2)| < 0.2$ is ignored.

4.3. Low-resolution structure images

The digitized image of a unit cell from fig. 2a, where the noise is filtered by averaging in accordance with the symmetry, is shown in the left of fig. 3. Large circular white places surrounded by six or seven black dots can be seen. The deconvoluted images by using a single image and by combining an image with the EDP are shown in the top right and bottom right, respectively. The determined defocus amount is −350 Å which is close to the Scherzer defocus [25] for the present accelerating voltage and spherical coefficient. This is the reason that the deconvoluted image is similar to the original image. The difference between the two images is that there are more black dots in the deconvoluted image than in the original image; for instance, all above mentioned circular white regions are occupied by one or more small black dots. In addition, at the center there is a black ring or a small black dot in the top and bottom images, respectively.

Fig. 4 shows the deconvolution result from the image shown in fig. 2b. Four large white disks surrounded by seven white dots and four triangular white dots surrounded by six white dots can be seen in the digitized image. The determined defocus amount is −850 Å which is far from the Scherzer defocus so that the image contrast changes drastically after image deconvolution. It is interesting that after image deconvolution all small circular and triangular white dots turn into black; four large white disks remain white but a

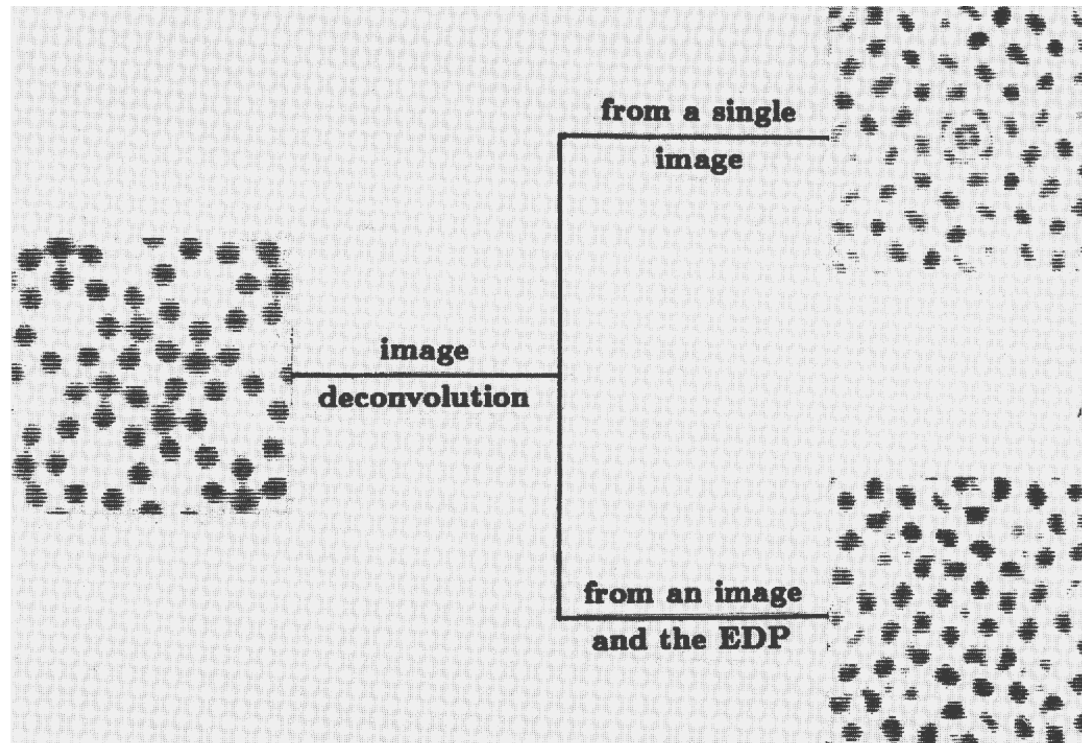

Fig. 3. Result of image deconvolution for image of $K_2O \cdot 7Nb_2O_5$ shown in fig. 2a. The digitized image of a unit cell is shown in the left. The deconvoluted images by using a single image and by combining an image with its corresponding EDP are shown in the top right and the bottom right, respectively.

large black dot with the shape of two circles being in contact with each other appears at the center in the top image and a small black dot appears at the center in the bottom image, respectively. Although there is some diffused contrast in the top image, the two deconvoluted images have a common contrast feature, and both are similar to the deconvoluted images shown in fig. 3. The fact that images taken under different defocus conditions and having much different contrast give similar deconvoluted images confirms the reliability of the maximum entropy method. These deconvoluted images in fact are restored structure images. Their resolution is limited by the resolution of electron microscopy. Therefore, it cannot be expected to see all atoms in these low resolution structure images. By comparing the two deconvoluted images in fig. 3 and in fig. 4 and by considering the crystallographical chemistry it can be seen that the image deconvolution by combining an image with the EDP gives a better result than that from a single image. In addition, as a structure image the bottom right image shown in fig. 4 seems to be more reasonable than that in fig. 3, because in the latter case some black dots are too close to each other. According to the chemical formula of the sample and the chemical crystallography the strong black dots in the structure images should represent Nb atoms and weaker black dots surrounded by six or seven strong black dots should represent K atoms. The dots at the origin and at the center of the unit cell seem to represent Nb atoms with atomic occupancy smaller than 1. O atoms do not appear in the image.

5. Determination of oxygen atoms by image resolution enhancement

5.1. High-resolution structure image obtained by phase extension using the direct method

Starting phases for the phase extension were derived from the low-resolution structure image shown in fig. 5a, which is the same image as

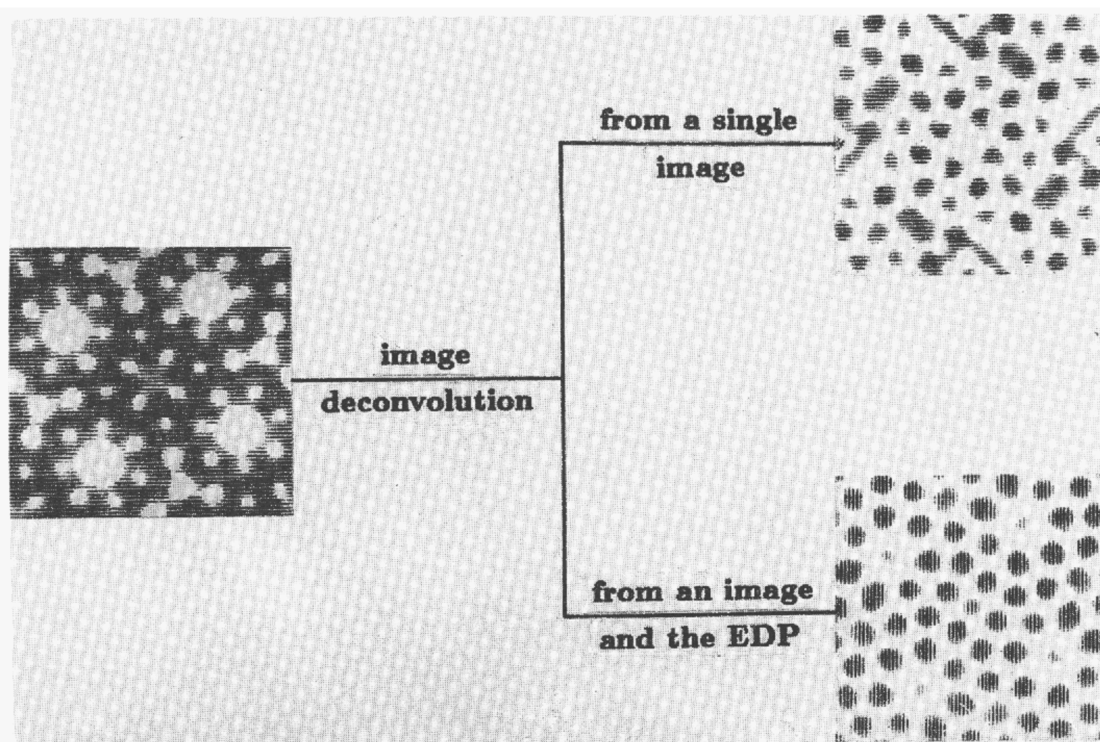

Fig. 4. Result of image deconvolution for image of $K_2O \cdot 7Nb_2O_5$ shown in fig. 2b. The digitized image of a unit cell is shown in the left. The deconvoluted images by using a single image and by combining an image with its corresponding EDP are shown in the top right and bottom right, respectively.

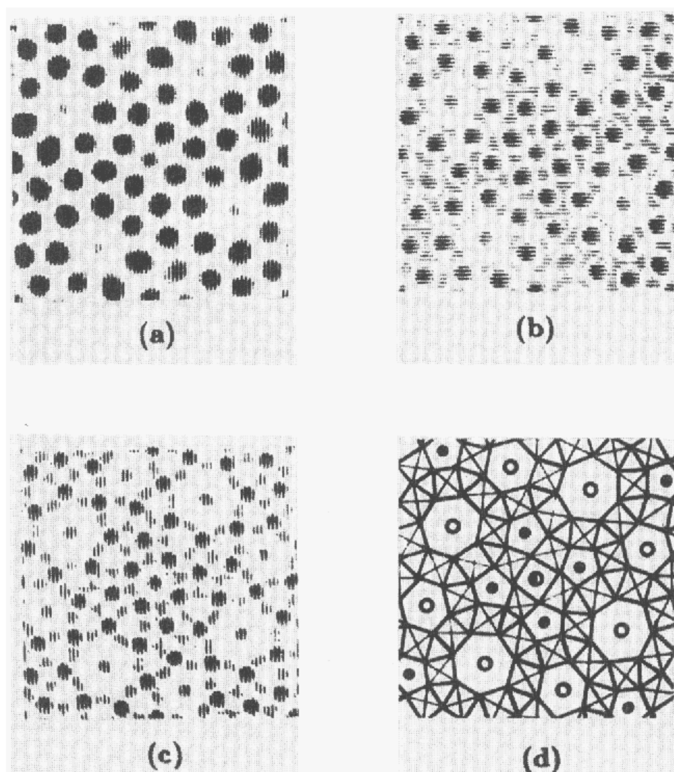

Fig. 5. (a) Low-resolution structure image of $K_2O \cdot 7Nb_2O_5$ of resolution 1.9 Å obtained from the image deconvolution. The determined defocus amount is −850 Å. (b) Initial high-resolution structure image obtained from (a) by phase extension. (c) Final high-resolution structure image obtained from (b) after three cycles of Fourier calculations. (d) Projected structure model constructed by referring to (c).

shown in the bottom right of fig. 4. The image resolution is 1.9 Å. The FT of the structure image yields phases of 636 reflections in the region of $H \leq (1.9\ \text{Å})^{-1}$. The number of independent reflections is 88. Among the 636 reflections there are 160 reflections with the corresponding absolute value of the CTF less than 0.2. The phases of these reflections were excluded from the starting phase set. Moduli of structure factors used in the phase extension were obtained from the electron diffraction intensity. Wilson statistics [24] was used to determine the overall temperature factors. The diffraction intensities were then put to the absolute scale by forcing the average intensity within a small interval of H to satisfy the following relation

$$\langle I(\boldsymbol{H}) \rangle_H = e^{-2B(\sin\theta/\lambda)^2} \sum_j f_j^2(\boldsymbol{H}), \tag{10}$$

where B is the overall temperature factor. This procedure is similar to the K-curve method [26] in X-ray crystallography for the calculation of normalized structure factors.

The phase extension was carried out simply by using the Sayre equation [27]

$$F(\boldsymbol{H}) = \frac{\theta}{V} \sum_{\boldsymbol{H}'} F(\boldsymbol{H}') F(\boldsymbol{H} - \boldsymbol{H}'), \tag{11}$$

where θ is the atomic form factor and V the volume of the unit cell. Structure factors of 476 reflections with the modulus obtained from the EDP and the phase from the structure image of resolution 1.9 Å were substituted into the right-hand side of eq. (11) to calculate the phases of 1844 reflections among which 1684 reflections are within the region of $(1.9\ \text{Å})^{-1} < H \leq 1\ \text{Å}^{-1}$ and the remaining 160 reflections are within $H \leq (1.9\ \text{Å})^{-1}$ and were rejected during the image deconvolution. A Fourier map, i.e. the inverse FT of structure factors, was calculated using moduli of structure factors from the electron diffraction intensity and the phases from the image deconvolution as well as from the phase extension. The result of the phase extension is shown in fig. 5b.

By comparing figs. 5a and 5b it can be seen that all peaks in fig. 5a appear also in fig. 5b, while there are more peaks in the latter. The large black dots in fig. 5a which are assumed to be Nb atoms remain as large black dots in fig. 5b. The dots inside hexagons and heptagons formed by Nb atoms are considered as K atoms. They are of different size in fig. 5a but have similar size in fig. 5b. In addition, in fig. 5b each large black dot is surrounded by four or five diffuse peaks which can be interpreted as O atoms. All of these indicate that the phase extension is successful, because all atoms including oxygen can be seen in fig. 5b. Hence, the map shown in fig. 5b is a structure image with the resolution higher than before phase extension.

5.2. Image quality improvement by successive Fourier synthesis

In order to further improve the image Fourier recycling was carried out. The positions of all

Table 1
A comparison of atomic positions determined in crystal of $K_2O \cdot 7Nb_2O_5$ and those in crystal $TlNb_7O_{18}$ given in ref. [30].

Atom	Site	$K_2O \cdot 7Nb_2O_5$		$TlNb_7O_{18}$ [30]	
		x/a	y/b	x/a	y/b
Nb(1)	2(d)	0.500	0.000	0.5000	0.0000
Nb(2)	4(g)	0.198	0.698	0.1986	0.6986
Nb(3)	8(i)	0.232	0.938	0.2328	0.9379
Nb(4)	8(i)	0.368	0.964	0.3678	0.9642
Nb(5)	8(i)	0.066	0.721	0.0664	0.7212
Nb(6)	8(i)	0.159	0.826	0.1583	0.8260
Nb(7)	8(i)	0.038	0.840	0.0382	0.8390
Nb(8)	8(i)	0.085	0.949	0.0864	0.9484
Nb(9)	2(b)	0.000	0.000	0.0000	0.0000
O(1)	2(c)	0.000	0.500	0.0000	0.5000
O(2)	4(h)	0.198	0.698	0.1976	0.6976
O(3)	8(j)	0.232	0.938	0.2280	0.9377
O(4)	8(j)	0.368	0.964	0.3653	0.9601
O(5)	8(j)	0.066	0.721	0.0652	0.7215
O(6)	8(j)	0.159	0.826	0.1575	0.8273
O(7)	8(j)	0.038	0.840	0.0381	0.8397
O(8)	8(j)	0.085	0.949	0.0791	0.9500
O(9)	4(g)	0.396	0.896	0.3992	0.8992
O(10)	8(i)	0.207	0.870	0.2082	0.8718
O(11)	8(i)	0.318	0.932	0.2997	0.9302
O(12)	8(i)	0.192	0.754	0.1954	0.7684
O(13)	8(i)	0.102	0.879	0.1044	0.8780
O(14)	8(i)	0.021	0.913	0.0208	0.9144
O(15)	8(i)	0.155	0.961	0.1562	0.9621
O(16)	8(i)	0.097	0.789	0.0944	0.7904
O(17)	8(i)	0.010	0.767	0.0107	0.7684
O(18)	8(i)	0.122	0.693	0.1271	0.6932
O(19)	8(i)	0.029	0.665	0.0277	0.6652
O(20)	8(i)	0.429	1.000	0.4283	0.9996
K(1)	4(h)	0.105	0.605	0.1084	0.6084
K(2)	4(h)	0.310	0.810	–	–

atoms were read from the peaks in fig. 5b. They were used to calculate the structure factors. The atomic scattering factors for electrons [28] were used in the calculation. Since the black dots located at the center and at vertices of the unit cell are smaller than other black dots which represent the Nb atoms, these black dots are considered to represent Nb atoms with smaller occupancy, for instance 0.5 or so. Again all the obtained phases of structure factors were used to calculate the inverse FT together with the moduli obtained from the electron diffraction intensity as mentioned above. In the resulting Fourier map the peaks of O atoms become sharper. Fig. 5c shows the final high-resolution structure image obtained after three cycles of Fourier calculation. All atoms including O atoms are resolved with the image contrast in accordance with the atomic weight. The atomic positions determined from this image are shown in table 1.

6. Structure model and simulated images

The high-resolution structure image shown in fig. 5c indicates that the crystal structure of $K_2O \cdot 7Nb_2O_5$ is isomorphous to that of $Rb_3Nb_{54}O_{146}$ [29], of $TlNb_7O_{18}$ [30] and also of $Cs_xNb_{54}(O.F)_{146}$ ($x \le 8$) [10]. Namely, the crystal consists of Nb–O octahedra which link one another by sharing vertices to form channels of different types as shown in the projected structure model (fig. 5d). The hexagonal and pentagonal channels are occupied by Nb atoms, the tetragonal and pentagonal channels are occupied by Nb atoms, and the triangular channels are unoccupied. The atomic occupancy of pentagonal, hexagonal and heptagonal equals unity, while that of tetragonal channels is smaller.

Table 2 shows the residual factors calculated with the formula

$$R = \frac{\sum || F_c(\boldsymbol{H}) | - | F_0(\boldsymbol{H}) ||}{\sum | F_c(\boldsymbol{H}) |}, \tag{12}$$

where $|F_0(\boldsymbol{H})|$ denotes the modulus of structure factor obtained from the electron diffraction intensity and $|F_c(\boldsymbol{H})|$ the moduli of structure factors calculated by using the atomic coordinates obtained from the final high-resolution structure image. The atomic occupancy inside the tetragonal channels was assumed to be equal to 0.5.

Images are simulated according to the determined structure model. It can be seen that the

Table 2
Residual factor R calculated after phase extension and different stages of Fourier synthesis

	phase extension	1st Fourier calculation	2nd Fourier calculation	3rd Fourier calculation
R	0.3871	0.3014	0.2863	0.2808

simulated images inserted in the bottom left of figs. 2a and 2b fit to the original images. Their defocus amounts are −300 and −830 Å, respectively. That the large white dots become smaller in the simulated image (fig. 2b) might be due to the effect of the exposure of emulsion grains to the electron beam.

7. Discussion and conclusion

The image deconvolution based on the principle of maximum entropy is efficient for transforming an image taken at defocus condition different from the structure image, and the combination of an image with the EDP gives better result than that from a single image alone. This means that the moduli of structure factors obtained from the electron diffraction intensity as a whole are more reliable than those obtained from the image, even when the EDP is not taken from the same sample area as the image. One of the reasons might be due to the oscillation of CTF. Great errors might occur for those structure factors which have $|\boldsymbol{H}|$ corresponding to a zero or very small value of CTF, when the structure factors are obtained from the Fourier transform of the image. The envelope of the CTF can also lead to such errors for large $|\boldsymbol{H}|$.

The deconvoluted image shown in the bottom right of fig. 4 is better than that of fig. 3. One possible reason is that the Fourier transform of the image shown in fig. 4 gives better phase information than that in fig. 3. In general, when the defocus amount is close to the Scherzer defocus, the CTF is not sensitive to small changes of defocus amount. This will result in a great error in the determination of defocus amount and hence lead to some error of phase information. This is in accordance with the result given in ref. [13].

The phase-extension technique developed in X-ray crystallography is efficient for image resolution enhancement. In principle the heavy-atom method can also be used for phase extension, once the positions of heavy atoms in the unit cell are known. Phases of all reflections in the EDP can be calculated approximately from the known position of the heavy atoms. A Fourier map using

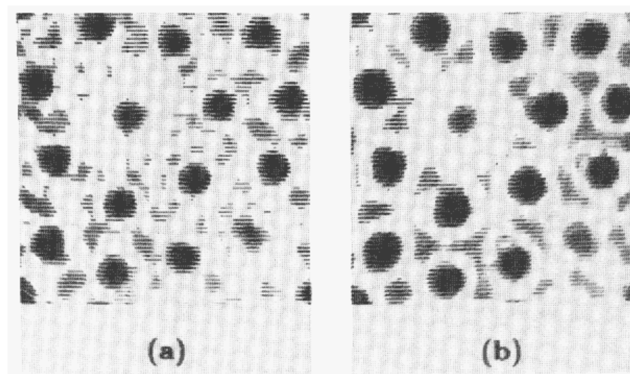

Fig. 6. Results of image resolution enhancement by (a) heavy-atom method and by (b) direct method. The map shows one fourth of the unit cell.

these phases will probably reveal at least some of the light atoms. The complete structure can then be obtained by Fourier recycling. Fig. 6 shows the Fourier map calculated with the moduli of structure factors from the electron diffraction intensity and the phases from the heavy atoms. Comparing fig. 6 with fig. 5b it is obvious that for the purpose of phase extension, the direct method is far better than the heavy-atom method in the present example.

By combining the structure information included in a high-resolution electron microscope image and the EDP and treating it by image deconvolution and by successive phase extension a new approach to crystal structure analysis is afforded.

Acknowledgement

The authors acknowledge Q.Z. Wu for providing the crystal of $K_2O \cdot 7Nb_2O_5$, Hitachi company, for allowing them to use the H-9000 high-resolution electron microscope, and Drs. F. Nagata and C. Tsuruta for helping to take the images. This project is partially supported by the National Natural Science Foundation of China.

References

[1] X. Wu, D.S. Tang, Z.M. Fu, Y. Fang, W.S. Li, X.L. Huang, M.X. Zhao and Q.Z. Wu, J. Synth. Cryst. 13 (1984) 95.

[2] F.H. Li, in: Proc. Int. Symp. on Electron Microscopy, Beijing, China, 22–23 October 1990 (World Scientific, Singapore, 1990) p. 300.
[3] D.L. Misell, J. Phys. D (Appl. Phys.) 6 (1973) L6.
[4] E.J. Kirkland, Ultramicroscopy 15 (1984) 151.
[5] E.J. Kirkland, B.M. Siegel, N. Uyeda and Y. Fujiyoshi, Ultramicroscopy 17 (1985) 87.
[6] D. Van Dyck and W. Coene, Optik 77 (1987) 125.
[7] P.N.T. Unwin and R. Henderson, J. Mol. Biol. 94 (1975) 425.
[8] A. Klug, Chem. Scripta 14 (1978-79) 245.
[9] S. Hovmöller, A. Sjögren, G. Farrants, M. Sundberg and B.-O. Marinder, Nature 311 (1984) 238.
[10] D.N. Wang, S. Hovmöller, L. Kihlborg and M. Sundberg, Ultramicroscopy 5 (1988) 303.
[11] N. Uyeda and K. Ishizuka, in: Proc. 8th Int. Congr. for Electron Microscopy, Vol. 1, Eds. J. Sanders and D. Goodchild (Australian Acad. Sci., Canberra, 1974) p. 322.
[12] F.H. Li and H.F. Fan, Acta Phys. Sinica 28 (1979) 276.
[13] F.S. Han, H.F. Fan and F.H. Li, Acta Cryst. A 42 (1986) 353.
[14] Y.W. Liu, S.B. Xiang, H.F. Fan, D. Tang, F.H. Li, Q. Pan, N. Uyeda and Y. Fujiyoshi, Acta Cryst. A 46 (1990) 459.
[15] J.J. Hu and F.H. Li, Ultramicroscopy 35 (1991) 339.
[16] F.H. Li, Acta Phys. Sinica 26 (1977) 245.
[17] K. Ishizuka, M. Miyazaki and N. Uyeda, Acta Cryst. A 38 (1982) 408.
[18] H.F. Fan, Z.Y. Zhong, C.D. Zheng and F.H. Li, Acta Cryst. A 41 (1985) 163.
[19] H.F. Fan, S.B. Xiang, F.H. Li, Q. Pan, N. Uyeda and Y. Fujiyoshi, Ultramicroscopy 36 (1991) 361.
[20] F.H. Li, C.M. Teng, J.J. Hu, F. Nagata and C. Tsuruta, in: Proc. 12th Int. Congr. on Electron Microscopy, Seattle, 1990, Vol. 1 p. 42.
[21] C.M. Teng, D.Y. Yang, F.H. Li and Q.Z. Wu, J. Chin. Silicate Soc. 15 (1987) 163.
[22] G. Bricogne, Acta Cryst. A 40 (1984) 410.
[23] F.H. Li and D. Tang, Acta Cryst. A 41 (1985) 376.
[24] A.J.C. Wilson, Acta Cryst. 8 (1949) 318.
[25] O. Scherzer, J. Appl. Phys. 20 (1949) 20.
[26] J. Karle, H. Hauptman and C.L. Christ, Acta Cryst. 11 (1958) 757.
[27] D. Sayre, Acta Cryst. 5 (1952) 60.
[28] J.S. Jiang and F.H. Li, Acta Phys. Sinica 33 (1984) 845.
[29] B.M. Gatehouse, D.J. Lloyd and B.K. Miskin, Natl. Bur. Stand. (US) Spec. Publ. 364 (1972) 15.
[30] V. Bhide and M. Gasperin, Acta Cryst. B 35 (1979) 1318.